Effect of ceria nanoparticles into the Pt/C catalyst as cathode material on the electrocatalytic activity and durability for low-temperature fuel cell

Dong-Ha Lim, Weon-Doo Lee, Dong-Hyeok Choi, Ho-In Lee *

School of Chemical and Biological Engineering and Research Center for Energy Conversion and Storage, Seoul National University, 599 Gwanangno, Gwanak-gu, Seoul 151-744, Republic of Korea

ABSTRACT

An effective method is developed for preparing highly dispersed CeO$_2$ nanoparticles on a Pt/C catalyst synthesized by a continuous two-step process as a cathode material in low-temperature fuel cell. The XRD patterns of the 20Pt–10CeO$_2$/C catalyst reveal that both crystalline Pt and CeO$_2$ phases coexist. The HR-TEM images show that Pt and CeO$_2$ nanoparticles have average particle sizes of approximately 3.4 nm and 4.2 nm, respectively, with quite a narrow distribution between 3 nm and 5 nm. Based on the analysis of the polarization curves for the ORR, the optimum proportion of CeO$_2$ into the 20Pt/C catalyst is 10 wt%. In the ORR and single cell tests, the 20Pt–10CeO$_2$/C catalyst shows higher performance than the commercial 20Pt/C catalyst, owing to the oxygen storage capacity of CeO$_2$ and its ability to exchange oxygen rapidly with oxygen in the buffer. In the accelerated stability tests, the 20Pt–10CeO$_2$/C catalyst has a better durability compared to the commercial 20Pt/C catalyst due to the existence of CeO$_2$, which prevents the agglomeration and dissolution of Pt nanoparticles on the carbon support, extending the life of the catalyst.

© 2009 Elsevier B.V. All rights reserved.

1. Introduction

Low-temperature fuel cell constitutes an attractive power source because of its high-energy efficiency, low-temperature operation, and zero-pollutant emission [1]. However, there are several problems such as high cost, poor durability, and low reliability to be solved to realize commercialization [2–6]. The high cost and durability are the major issues, and the efficiency of performance should be further improved. The high cost of Pt catalyst, which is the best single metal catalyst, has been one of the several obstacles hindering the commercialization of a low-temperature fuel cell. Thus, to produce a useful electrocatalyst, the amount of Pt catalyst in the electrodes should be minimized but without decreasing catalytic activity to achieve a competitive low cost. In addition, fuel cell durability has also been one of the major issues to be solved to realize commercialization [2–4]. Especially, the loss of fuel cell performance has been attributed to the remarkable decrease of electrochemical active surface area (EAS) of Pt catalyst in the cathode, due to low pH ($<\sim$1), high potential (0.6–1.2 V), high oxygen concentration (20–100%), high humidity, and high temperature ($\sim$80 °C) [7,8].

The agglomeration and dissolution of the Pt catalyst in the cell operation condition bring about the decrease of the Pt surface area, and hence the fuel cell performance is significantly decreased. In the last decade, significant efforts have been made on lowering the load of Pt or finding substitutes of Pt to reduce the electrode cost and improve upon the performance and durability in a fuel cell system [9–21]. Improving the catalytic activity at the cathode, where oxygen reduction reaction (ORR) occurs, is crucial to increase overall efficiency of low-temperature fuel cell, because most of the performance losses are due to the slow cathode kinetics [22–24]. To improve the catalytic activity at the cathode, research has been mainly focused on the development of new catalyst materials including noble and non-noble metals with high catalytic activity, utilization efficiency, and durability.

Some solutions to the above mentioned problems that were introduced involve the development of binary Pt alloys such as PtNi, PtCo, PtFe to enhance the ORR activity and reduce the Pt content [24–28]. Although the alloy catalysts showed improved ORR activity compared to a Pt/C catalyst, their stabilities were still poor. Recently, the Pt/C catalyst with adding metal oxides has been extensively investigated for enhancing the ORR activities [22,23,29–36]. The addition of metal oxides into the cathode has been studied to facilitate the supply of oxygen species leading to enhanced fuel cell performance [22,23,29–34].

* Corresponding author. Tel.: +82 2 880 7072; fax: +82 2 888 1604.
E-mail address: hilee@snu.ac.kr (H.-I. Lee).

Especially, ceria (cerium oxide, CeO_2), one of the most widely used rare earth metal oxide as a promoter for metallic catalysts, has been extensively applied in three-way catalysts, water–gas-shift reaction, fuel cells, solar cells [22,23,29–34]. CeO_2 is a fluorite-structured oxide with high oxygen storage capacity (OSC) associated with its rich oxygen vacancies and low redox potential between Ce^{3+} and Ce^{4+}, as well as electrical property [37–44]. In addition, CeO_2 tends to interact with the active components, which may result in high dispersion of the active species [37–39]. Recently, CeO_2 has been investigated as a promoter into the Pt/C catalyst for enhancing catalytic activity in low-temperature fuel cell due to its unique properties [22,23,29–34]. Lee et al. [23] recently reported that PtCo–CeO_x/C catalyst prepared by modified colloid method had higher ORR activity than PtCo/C catalyst due to an enhanced oxygen supply to the PtCo alloys. Xu et al. [34] showed that the addition of CeO_2-based materials into a Pt/C catalyst slightly enhanced the cell performance at lower cell voltages (e.g. higher current densities). They reported that CeO_2-based materials, which have the ability to store oxygen, could provide additional oxygen to Pt active sites. A Japanese patent [33] reported that adding CeO_2-based materials into the cathode largely increased air utilization at 0.6 V. Our groups have reported that a commercial Pt/C catalyst physically mixed with CeO_2 for the cathode has been shown to increase the local oxygen concentration in the air atmosphere, leading to an enhanced cell performance in direct methanol fuel cell [31]. It seems reasonable to expect that if such oxygen storage material was incorporated into the cathode, local oxygen concentration would be increased. This could in turn enhance the cell performance. However, the previous work did not address the kinetics of ORR and the durability issue for low-temperature fuel cell.

In this study, in order to look for more active and more durable cathode material synthesized by a continuous two-step process, we have been studying the effect of CeO_2 as a promoter into the Pt/C catalyst for structural characterization, ORR activity, durability, and single cell performance. We also propose a reasonable scheme of improving cell performance for the addition of CeO_2 into the Pt/C catalyst as cathode in low-temperature fuel cell.

2. Experimental

2.1. Catalyst preparation

The 20Pt–$xCeO_2$/C catalysts, which would be used as the cathode in low-temperature fuel cell, was prepared by the following continuous two-step process: first, nano-sized CeO_2 particles deposited on a carbon support were prepared by hydrothermal treatment. Then the chemical reduction of a Pt metal salt, which was added to the dissolved CeO_2/C solution, was carried out by borohydride reduction. The loading amount of Pt metal in the hand-made and commercial (E-TEK) catalysts was fixed by 20 wt% in this study. The following were quantitatively dissolved into 100 ml of distilled water in a Teflon bottle: 0.002 g, 0.012 g, 0.024 g, and 0.036 g of cerium(III) chloride heptahydrate ($CeCl_3 \cdot 7H_2O$, Aldrich) (which correspond to 1 wt%, 5 wt%, 10 wt%, and 15 wt% CeO_2/C, respectively) and 0.1 g of carbon black (Vulcan XC-72R, Cabot Co.) pretreated with 60% nitric acid at its boiling point (140 °C). 5 M NaOH solution was then slowly added until the pH reached 11. The Teflon bottle was placed in a stainless steel vessel and sealed tightly. To crystallize the CeO_2, the hydrothermal process employs high temperatures and high pressures. The hydrothermal treatment was performed in an oven at 150 °C for 10 h, and then the autoclave was cooled down to room temperature. Next, 0.066 g of chloroplatinic acid ($H_2PtCl_6 \cdot 6H_2O$, Acros Organics) was added to the prepared CeO_2/C solution. With vigorous stirring, 0.01 g of sodium borohydride ($NaBH_4$, Junsei

Chemicals) dissolved in 30 ml of H_2O was added drop-by-drop to the solution. After this reduction, the solution was treated by adding 5 M HCl solution until the pH reached 2. The resulting suspension was filtered, washed with excess ethanol and distilled water, and then dried overnight in a vacuum oven at room temperature. The samples were characterized by Braunauer–Emmett–Teller (BET) analysis, electric conductivity, X-ray diffraction (XRD), high resolution-transmission electron microscopy (HR-TEM), energy dispersive X-ray spectroscopy (EDS) thermogravimetry differential scanning calorimetry (TG-DSC), temperature programmed reduction (TPR), and evaluated with electrochemical techniques.

2.2. Physical characterizations

The specific surface areas of the catalysts were calculated based on a multipoint Braunauer–Emmett–Teller (BET) analysis of the nitrogen adsorption isotherms recorded using a surface area analyzer (ASAP 2020, Micromeritics). The electric conductivity of the catalyst was measured using a four-point probing system (Model 2400 SourceMeter, Keithley). Structural characteristics of the synthesized powders were investigated by XRD (D8 ADVANCE, Bruker) using Cu $K\alpha$ as the radiation source. For XRD, the working voltage and current were maintained at 40 kV and 30 mA, respectively. The 2θ angular region between 20° and 60° was explored at a scan rate of 0.2 s $step^{-1}$. The surface morphology of Pt and CeO_2 nanoparticles on carbon black was studied using HR-TEM (JEM-3010, JEOL) operated at 300 kV. The TEM samples were prepared by adding a drop of the suspension, made by ultrasonically dispersing the catalyst in ethanol, on a copper grid covered with carbon film, and then evaporating the ethanol. An EDS fitted to the TEM was used for elemental analysis. For temperatures ranging from 30 °C to 800 °C in an air flow of a 100 ml min^{-1}, the TG-DSC measurement was conducted using a thermal analyzer (SDT Q-600, TA Instruments) with an alumina sample pan. The TPR (BEL-CAT, BEL) was done using a fixed-bed tubular reactor unit equipped with a thermal conductivity detector. A flow of 5% H_2 in Ar at 25 ml min^{-1} was used to reduce the catalyst while raising the temperature from 25 °C to 1000 °C at a heating rate of 10 °C min^{-1}.

2.3. Electrochemical measurements

Electrochemical measurements were carried out in a half-cell using a potentiostat (PC4/750, Gamry Instruments). The catalytic activity for the ORR was measured with a rotating disk electrode (RDE) (AFMSRX modulated speed rotator, Pine Instruments) installed with a glassy carbon (GC) RDE tips (AFE3T050GC, Pine Instruments). A conventional three-electrode cell, in which reference, counter, and working electrodes were separated, was used for the ORR test over the 20Pt–10CeO_2/C catalyst and commercial 20Pt/C catalyst in 0.5 mol l^{-1} H_2SO_4 electrolyte solution. The catalyst ink was prepared by ultrasonicating the catalyst with 5 wt% Nafion® (1100 EW, Du Pont) in isopropyl alcohol for approximately 30 min to form a slurry. The ratio of catalyst to Nafion® in the catalyst ink was 3:1. A GC RDE tips with a diameter of 5 mm, which were polished to a mirror finish with a 0.05 μm gamma alumina suspension (40-6301-016, Buehler) before each experiment, was used as the substrate for the catalyst ink. A drop of catalyst ink was pipetted onto the surface of the GC RDE tips and dried at room temperature. Each electrode was installed into a three-electrode cell with a platinum mesh electrode (219810, Princeton Applied Research) as counter electrode and a KCl-saturated Ag/AgCl electrode (MF-2052, Bioanalytical System, Inc.) as the reference electrode, which was located as close as possible to the working electrode. The three-electrode cell was filled with the electrolyte solution and purged with nitrogen gas to remove oxygen dissolved in the electrolyte solution. All the potential

readings were recorded with respect to a normal hydrogen electrode (vs. NHE). Before all electrochemical measurements, the potential was cycled between +0 V and 1.2 V at 100 mV s^{-1}, to obtain a clean, active electrochemical surface. The RDE curves were obtained in the scan range from 1.0 V to 0.4 V (vs. NHE) with a scan rate of 50 mV s^{-1} after oxygen bubbling for 20 min.

2.4. Fuel cell testing

The membrane electrode assembly (MEA) for the low-temperature fuel cell was fabricated from Nafion® 112 membrane (DuPont) as described elsewhere [45]. The membrane was pretreated by successive dipping at 80 °C for 30 min each step in 5 wt% H_2O_2 solution, distilled water, 8 wt% H_2SO_4 solution and then in distilled water again. For preparation of the catalyst-coated membrane, the catalyst ink was sprayed uniformly by a spray gun onto the pretreated membrane. The catalyst loading of anode and cathode was both 0.3 mg cm^{-2}, and the active surface area of the single cell was 5 cm^{-2}. A gas diffusion layer, based on carbon paper substrates (TGPH-060, Toray Inc.), was placed on the anode and the cathode sides of the catalyst-coated membrane to form a single cell. The cell operating temperature was set at 80 °C. The flow rates of humidified H_2 and O_2 gas were 100 cm^3 min^{-1} and were controlled with a flowmeter. I–V curves were obtained galvanostatically with an electronic load (EL200P, Daegil). The performance of these MEAs was evaluated with a commercial fuel cell test station (SMART II PEM/DM Hybrid Fuel Cell Test System, WonATech Co.).

3. Results and discussion

3.1. Physical characterization

BET surface areas and electric conductivities of the pretreated carbon, as well as Vulcan XC-72R, are shown in Fig. 1. The BET surface area and electric conductivity of carbon pretreated for 1 h are 215 m^2 g^{-1} and 1.18 S cm^{-1}, respectively. These values of the pretreated carbon are similar to those of carbon black, while for carbon pretreated for 2 h and 3 h, these values sharply decrease. The depositions of CeO_2 and Pt nanoparticles cause a decrease in the specific surface area. The specific surface areas of the 20Pt–xCeO$_2$/C catalysts prepared using hydrothermal treatment with subsequent borohydride reduction are shown in Table 1.

Fig. 2 shows the X-ray diffraction patterns of xCeO$_2$/C (x = 1, 5, 10, 15) powders synthesized by hydrothermal treatment at 150 °C for 10 h; this resulted in several new peaks. There are four CeO$_2$ diffraction peaks of 1 1 1, 2 0 0, 2 2 0, and 3 1 1 with phases at

Table 1
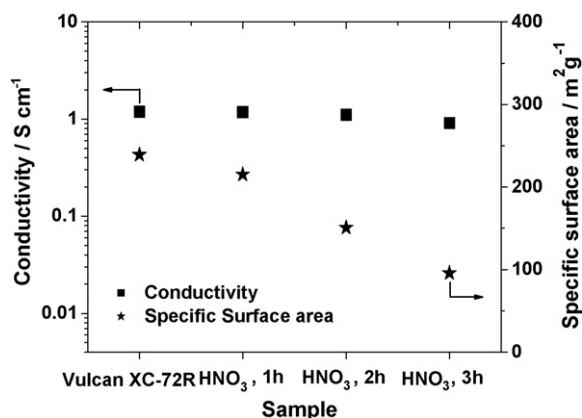Comparison of the BET surface areas of xCeO$_2$/C and 20Pt–xCeO$_2$/C catalysts prepared using hydrothermal treatment with subsequent borohydride reduction.

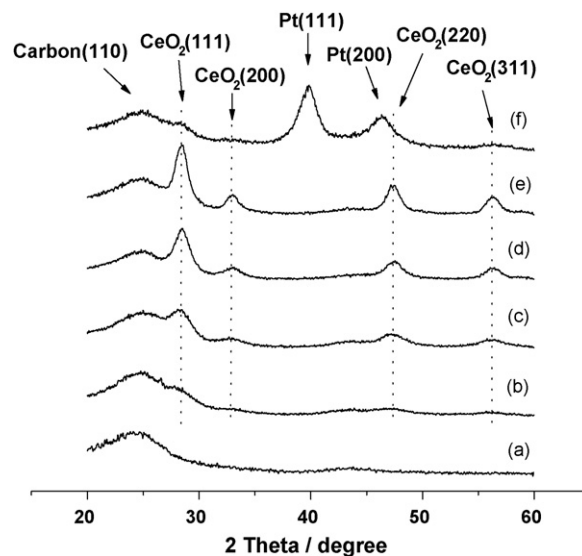| Sample	Specific surface area (m^2 g^{-1})
Treated carbon	215
1CeO$_2$/C	203
5CeO$_2$/C	196
10CeO$_2$/C	175
15CeO$_2$/C	151
20Pt/C	193
20Pt–1CeO$_2$/C	184
20Pt–5CeO$_2$/C	156
20Pt–10CeO$_2$/C	134
20Pt–15CeO$_2$/C	113

Fig. 2. X-ray diffraction patterns of the (a) treated carbon, (b) 1CeO$_2$/C, (c) 5CeO$_2$/C, (d) 10CeO$_2$/C, (e) 15CeO$_2$/C, and (f) 20Pt–10CeO$_2$/C catalysts.

28.6°, 33.1°, 47.5°, and 56.3°, respectively. These diffraction peaks index as CeO$_2$ with cubic fluorite structure, in good agreement with literature values [38,39]. It can be seen from Fig. 2 that, with larger amounts of CeO$_2$ deposited on carbon, the CeO$_2$ peaks are more prominent. Scherrer's equation is used to estimate the average crystallite size. The 10CeO$_2$, 5CeO$_2$, and 1CeO$_2$ nanoparticles supported on carbon, which show average crystallite sizes of about 4.5 nm, 3.8 nm, and below the detection threshold, respectively, are readily synthesized using hydrothermal treatment. The liquid phase reduction of Pt salt, which is added to the dissolved CeO$_2$/C solution, is subsequently carried out with borohydride reduction. It is evident from the diffraction pattern of the 20Pt–10CeO$_2$/C catalyst, shown in Fig. 2f, that both crystalline Pt and CeO$_2$ phases coexist. It is clearly seen that no shift in the positions of the Pt diffraction peaks is noted for the 20Pt–10CeO$_2$/C catalyst. This indicates that the added CeO$_2$ into the Pt/C catalyst has no effect on the crystalline lattice of Pt. The average crystallite size of Pt is around 3.2 nm for the 20Pt–10CeO$_2$/C catalyst. Scibioh et al. [40] reported that the XRD patterns of Pt–CeO$_2$/C catalyst show no shift in the Pt diffraction peaks at all compositions, indicating that there is no alloy formation between Pt and CeO$_2$.

To confirm well-dispersed CeO$_2$ nanoparticles deposited on carbon surface, the CeO$_2$/C was firstly synthesized by hydrothermal treatment before second step with borohydride reduction. As shown in Fig. 3a, it is clearly seen that well-dispersed, uniform CeO$_2$ nanoparticles with an average particle size of around 4.2 nm can be found on the surface of the carbon support. Considering the similar sizes of CeO$_2$ estimated from XRD and TEM data, each
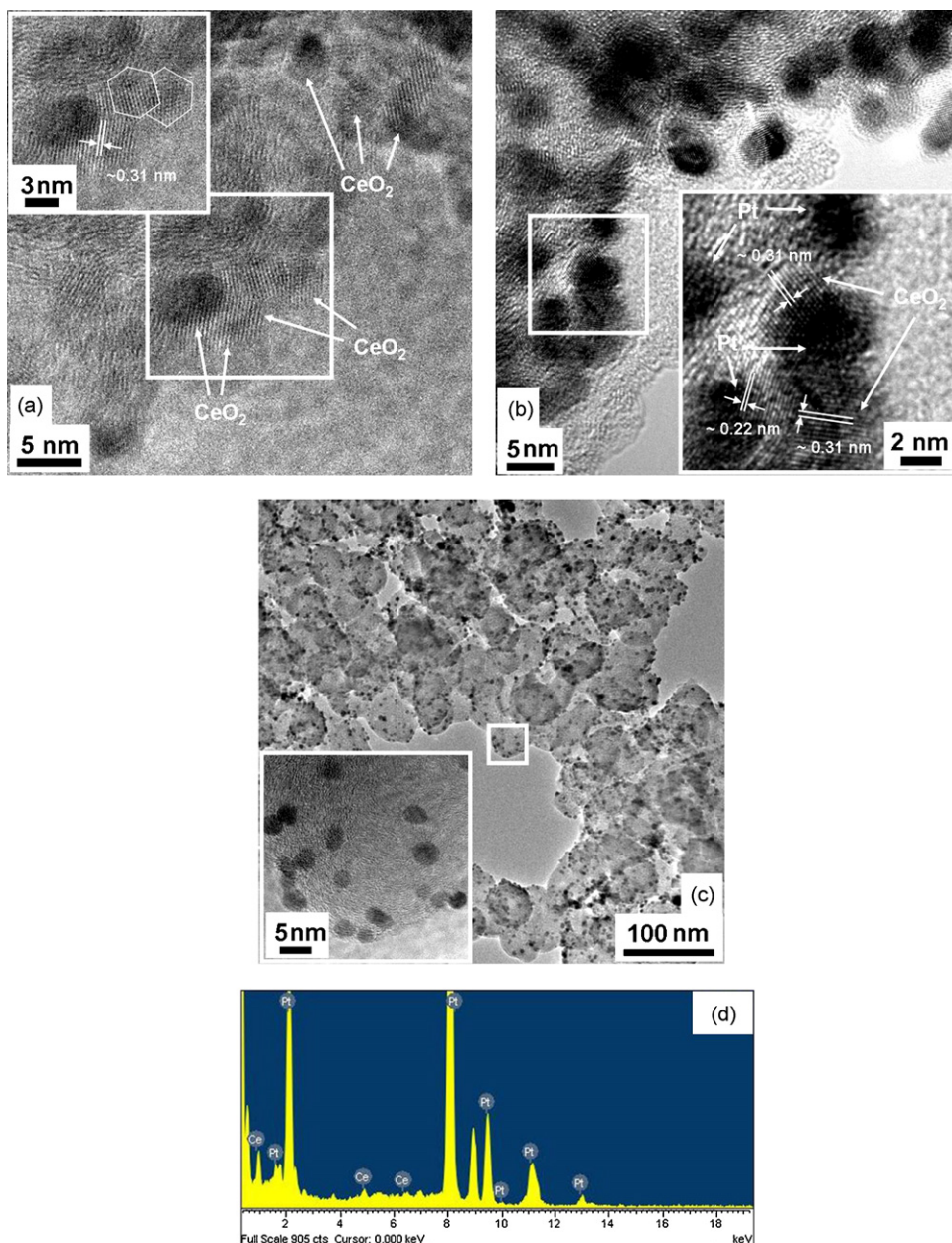

Fig. 1. Comparison of the conductivity and specific surface area of carbon treated for different time and Vulcan XC-72R.

Fig. 3. HR-TEM images of the (a) $10CeO_2/C$ and (b and c) $20Pt–10CeO_2/C$ catalysts and (d) EDX pattern for the $20Pt–10CeO_2/C$ catalyst.

crystallite seems to form an individual particle. In addition, the uniformly deposited CeO_2 nanoparticles on the carbon support play an important role in the dispersant for the subsequent highly deposited Pt nanoparticles and the contact between Pt and CeO_2 particles. In Fig. 3b, we can clearly see two cases of Pt nanoparticles supported on the carbon surface. One case is that some Pt nanoparticles are deposited on the carbon surface with no contact with CeO_2 nanoparticles. Another case is that others have contact with CeO_2 nanoparticles. Especially, CeO_2 nanoparticles can be found near Pt nanoparticles, as the crystal phases of Pt and CeO_2 are identified by lattice analysis. The lattice spacing of Pt and CeO_2 was ~0.22 nm and ~0.31 nm corresponding to Pt(1 1 1) and CeO_2(1 1 1), respectively [41]. We can also confirm from Fig. 3c that Pt and CeO_2 nanoparticles are uniformly dispersed on the edge of the carbon support, and no obvious agglomeration of metal particles is shown. The EDS spectrum (Fig. 3d) of the $20Pt–10CeO_2/$ C catalyst proves the coexistence of Pt and Ce on the carbon support. Therefore, Pt–CeO_2/C catalysts, which are CeO_2 nanopar-

ticles closed to Pt active sites, were successfully synthesized via a continuous two-step process.

Fig. 4 presents the TEM images of the $20Pt–xCeO_2/C$ catalysts (x = 1, 5, 10, 15) prepared by a continuous two-step process. It can be clearly seen from Fig. 4 that the Pt and CeO_2 particles are homogeneously dispersed on the carbon support with no obvious aggregations in the $20Pt–xCeO_2/C$ catalysts (except $20Pt–15CeO_2/$ C). The addition of 10 wt% CeO_2 into the Pt/C catalyst leads to a slight decrease of the Pt particle size among the prepared samples, as witnessed in TEM images (Fig. 4c). We believe that smaller Pt particles in the $20Pt–10CeO_2/C$ catalyst could be attributed to the presence of well-dispersed CeO_2 nanoparticles. Scibioh et al. [40] insisted that addition of CeO_2 into the Pt/C catalyst leads to a little decrease of the average Pt particle size. On the other hand, in the case of the $20Pt–15CeO_2/C$ catalyst, severe agglomeration of the particles on the carbon support is observed (Fig. 4d). The order of the Pt particle size is as follows: $20Pt–10CeO_2/C < 20Pt–5CeO_2/$ C $< 20Pt–1CeO_2/C < 20Pt–15CeO_2/C$. We believe that smaller the
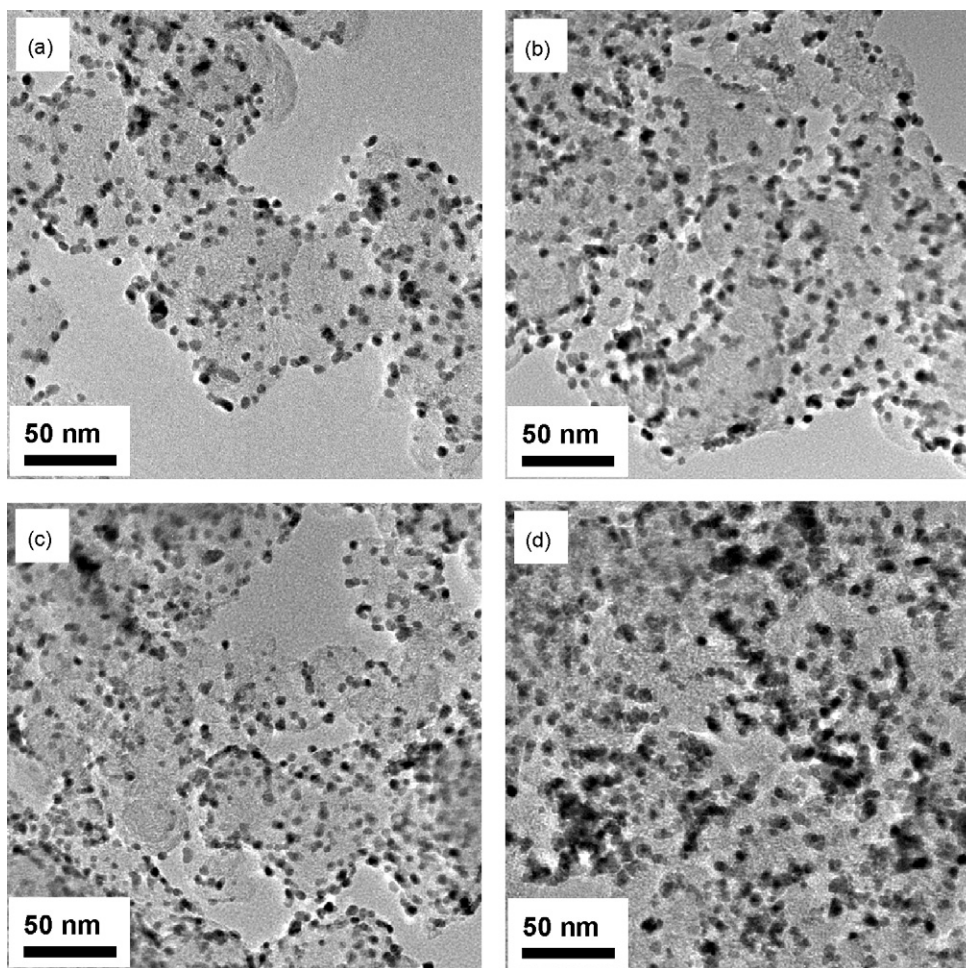
Fig. 4. The images of the (a) 20Pt–1CeO$_2$/C, (b) 20Pt–5CeO$_2$/C, (c) 20Pt–10CeO$_2$/C, and (d) 20Pt–15CeO$_2$/C catalysts.

Pt particles, the higher Pt surface area can come in contact with CeO$_2$ particles. Thus, in the case of 20Pt–10CeO$_2$/C, it is possible to obtain the highest synergism between the metal and the oxide with the highest number of Pt particles in contact with CeO$_2$ particles, resulting in improving ORR activity and durability.

Fig. 5a shows the TG-DSC curve of the 20Pt–10CeO$_2$/C sample. The first peak below 180 °C can be attributed to the removal of physisorbed water and structural water from the catalyst. The second peak at about 300 °C can be attributed to the removal of some carbon species' functional groups. The peaks with a dramatic weight loss at about 400 °C and 450 °C are due to the combustion of carbon to form CO$_2$. The combustion is completed at about 550 °C and leaves about 29.2% of the sample as residue due to the supported Pt and CeO$_2$. In addition, the loading amounts of the 20Pt–1CeO$_2$/C, 20Pt–5CeO$_2$/C, and 20Pt–15CeO$_2$/C catalysts are 20.8%, 23.8%, and 30.4%, respectively (not shown). Based on the TGA results, the loading amounts of Pt and CeO$_2$ are confirmed to be accurate. Thus, the method employed guarantees the complete preparation of Pt and CeO$_2$, as well as the full loading of Pt and CeO$_2$ nanoparticles on a carbon support. Furthermore, it can be seen from Fig. 5b that the dramatic weight loss for 20Pt–10CeO$_2$/C occurs at lower temperature compared to 10CeO$_2$/C and shows a relatively gentle slope in comparison with the commercial 20Pt/C. The lower temperature and the gentle slope of the dramatic weight loss are due to the existence of Pt metal closed to CeO$_2$ particles, suggesting that the Pt nanoparticles catalyzed the oxidation of carbon.

In order to further evaluate the contact between Pt and CeO$_2$, the reducibility of the treated carbon, 20Pt/C, 10CeO$_2$/C, 20Pt–

5CeO$_2$/C, and 20Pt–10CeO$_2$/C catalysts is evaluated by conventional hydrogen TPR experiments, as shown in Fig. 6. It is well known that the TPR profile of CeO$_2$ has two hydrogen consumption peaks associated with the reduction of surface and bulk oxygen [42–44]. From the TPR profile of CeO$_2$/C, the first peak at low-temperature (320 °C) is attributed to the reduction of surface oxygen. The second peak at high temperature (640 °C) is associated with the reduction of bulk oxygen. The TPR profile of CeO$_2$/C shows higher intensity and lower temperature than that of the treated carbon, which is associated to the reduction of surface and bulk CeO$_2$ with high dispersion on carbon. The TPR profiles of the 20Pt–5CeO$_2$/C and 20Pt–10CeO$_2$/C catalysts show that the peaks associated with both surface and bulk oxygen reductions shifted to lower temperatures in comparison with that of 10CeO$_2$/C. This is because well-dispersed Pt and CeO$_2$ nanoparticles are present on the carbon surface, as witnessed in Fig. 3c. Serrano-Ruiz et al. [42] reported that two big overlapped peaks in the TPR profile of the Pt/CeO$_2$/C shift to lower temperature. The peak at lower temperature can be assigned to the surface reduction of CeO$_2$ in close contact with Pt, this accounting for a strong interaction between Pt and CeO$_2$ [42]. Furthermore, the second main peak for the 20Pt–10CeO$_2$/C and 20Pt–5CeO$_2$ catalysts shows two overlapping peaks of bulk oxygen reduction as the front peak (530 °C and 560 °C) and the shoulder peak (620 °C and 645 °C). Therefore, we believe that the front peak of bulk oxygen reduction is probably due to the interaction between Pt and adjacent CeO$_2$ nanoparticles; however, the shoulder peak appears to be from the reduction of bulk oxygen in the separated Pt and CeO$_2$ nanoparticles.
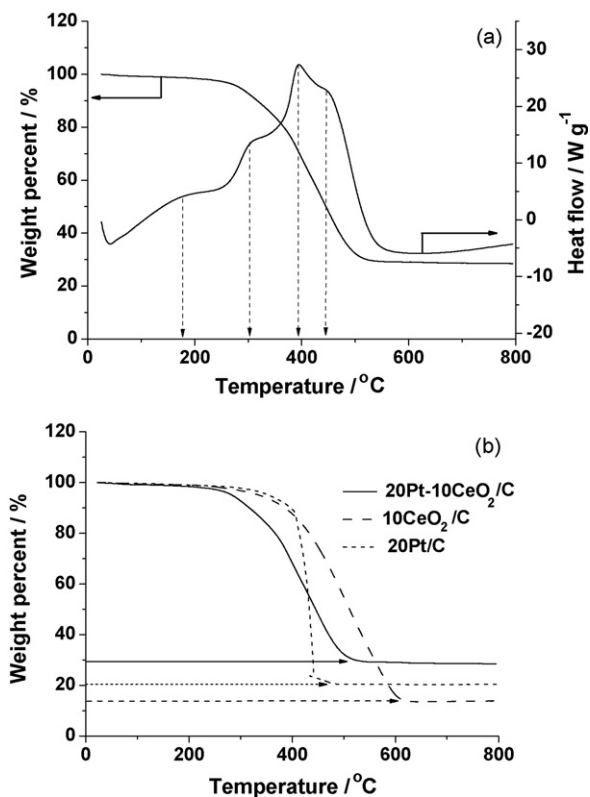
Fig. 5. (a) TG-DSC curve of the 20Pt–10CeO$_2$/C catalyst and (b) TG curves of the 20Pt–10CeO$_2$/C, 10CeO$_2$/C, and 20Pt/C catalysts.
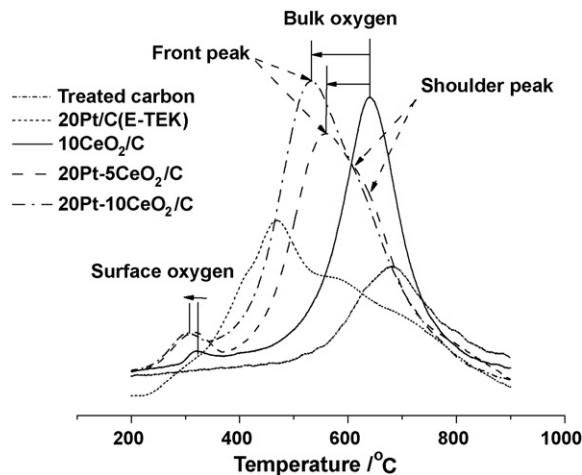

Fig. 6. TPR profiles of the treated carbon, 20Pt/C, 10CeO$_2$/C, 20Pt–5CeO$_2$/C, and 20Pt–10CeO$_2$/C catalysts.

3.2. Electrocatalytic activity for oxygen reduction reaction (ORR)

The 20Pt–xCeO$_2$/C (x = 1, 5, 10, 15) catalysts are investigated by RDE voltammetry as described in Section 2 to study the content of the CeO$_2$ into the Pt/C catalyst for the ORR activity of the prepared catalyst. The content of the CeO$_2$ should be added into the Pt/C catalyst to accomplish the best ORR activity because CeO$_2$ is not a main active site and a good electrical conductor. As shown in Fig. 7, the addition of CeO$_2$ into the Pt/C catalyst (except 20Pt–15CeO$_2$/C) shows higher kinetic current density per milligram of Pt metal and half-wave potential ($E_{1/2}$) for the ORR with respect to the commercial 20Pt/C catalyst. The ORR activity shows a volcano
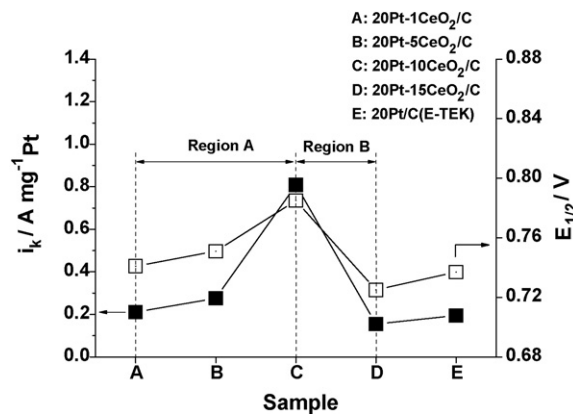

Fig. 7. Changes of kinetic current density per milligrams of Pt metal at 0.75 V and half-wave potential ($E_{1/2}$) obtained on the 20Pt–xCeO$_2$/C and commercial 20Pt/C(E-TEK) catalysts in 0.5 mol l^{-1} H$_2$SO$_4$ saturated with pure oxygen. Scan rate = 50 mV s^{-1} at 3600 rpm.

Table 2
Electrokinetic parameters on the 20Pt–10CeO$_2$/C and commercial 20Pt/C catalysts from RDE measurements in 0.5 mol l^{-1} H$_2$SO$_4$ saturated with pure oxygen at 3600 rpm.

Sample	EAS$_{H_2}$ (m^2 g^{-1})	$E_{1/2}$ @ 3600 rpm (mV)	i_k @ 0.75 V (mA mg$^{-1}_{Pt}$)	i_k @ 0.75 V (μA cm$^{-2}_{Pt}$)
20Pt/C(E-TEK)	42.4	737	195	460
20Pt–1CeO$_2$/C	43.6	741	211	470
20Pt–5CeO$_2$/C	45.7	751	276	550
20Pt–10CeO$_2$/C	49.4	785	809	1420
20Pt–15CeO$_2$/C	38.2	725	155	409

curve and the optimum proportion of CeO$_2$ into the 20Pt/C catalyst is 10 wt%. The order of the ORR activity is as follows: 20Pt–10CeO$_2$/C > 20Pt–5CeO$_2$/C > 20Pt–1CeO$_2$/C > 20Pt–15CeO$_2$/C. Furthermore, we confirm from Table 2 that the order of the ORR activity follows EAS values. It is well known that EAS values of the catalysts are one of the important factors to evaluate the ORR activity. The 20Pt–10CeO$_2$/C catalyst with the highest EAS value shows the best catalytic activity for ORR among the prepared samples. However, for the 20Pt–15CeO$_2$/C, an excessive amount of CeO$_2$ leads to significant decrease of EAS values and thus, to decrease of ORR activity. Higher EAS value of the 20Pt–10CeO$_2$/C catalyst is due to the presence of well-dispersed Pt nanoparticles on the carbon support, as witnessed in TEM image (Fig. 3c).

We considered that the changes of the ORR activity with CeO$_2$ content into the Pt/C catalyst. For the dependency of the ORR activity, we divided the ORR activity dependence into two regions of A and B, as shown in Fig. 7. In the case of 'region A', the ORR activity of 20Pt–xCeO$_2$/C catalysts (x = 1, 5, 10) is higher than that of the commercial 20Pt/C catalyst. Especially, the 20Pt–10CeO$_2$/C catalyst shows the best catalytic activity for the ORR among those prepared. Contacts between Pt and CeO$_2$ nanoparticles in the 20Pt–10CeO$_2$/C catalyst could be more than the others, as shown in Fig. 4c. The appropriate existence of CeO$_2$ in the vicinity of Pt nanoparticles may act as a promoter for the ORR rather than as active site itself (synergistic effect). Therefore, more synergistic ORR between both nanoparticles would occur on their interfaces, where a large amount of oxygen supply is possible when compared with the others, thus improving ORR activity. On the other hand, in the 'region B' with 15 wt% CeO$_2$ content, the ORR activity shows the lowest among the prepared catalysts in this study. This would be due to a decrease of the Pt surface area as main active site (Table 2) and an excessive amount of CeO$_2$, which decrease an electrical conductivity of the catalyst and which does not act as a promoter

for the ORR at this CeO_2 content. From the experimental findings, there is a critical value of CeO_2 content, up to which the ORR activity increases due to the CeO_2 formed at the adjacent to Pt nanoparticles, but above which the ORR activity decreases due to the decrease of the Pt active area and the decrease of electrical conductivity. Consequently, in this study, the optimum value of CeO_2 content was 10 wt% resulted from 20Pt–10CeO_2/C catalyst which gave the best ORR activity as shown in Fig. 7.

In order to see the effect of CeO_2 into the Pt/C catalyst, it is necessary to compare the ORR activity of 20Pt–10CeO_2/C and commercial 20Pt/C catalysts. Fig. 8a shows the polarization curves of the 20Pt–10CeO_2/C and commercial 20Pt/C catalysts for the ORR activity obtained at 25 °C in 0.5 mol l^{-1} H_2SO_4 electrolyte solution saturated with oxygen using RDE at a rotation rate of 3600 rpm; it compares the ORR activity in $E_{1/2}$ of the 20Pt–10CeO_2/C catalyst with that of the commercial 20Pt/C catalyst. It is clear that the $E_{1/2}$ of the 20Pt–10CeO_2/C catalyst (0.785 V) shows significantly an anodic shift of about 50 mV in the mixed kinetic-diffusion controlled region compared to that of the commercial 20Pt/C catalyst (0.736 V) and consequently about 50 mV lower over-potentials for the ORR. And also, the onset potential of the ORR is higher on the 20Pt–10CeO_2/C catalyst than on the commercial 20Pt/C catalyst. This is because the CeO_2 acts as an oxygen buffer to Pt particles for the reduction of oxygen. CeO_2 could transfer oxygen to Pt nanoparticles, resulting in much better ORR activity (synergistic effect). According to CeO_2 redox properties (Ce^{3+}/Ce^{4+} balance), it can store O_2 during an oxygen-rich phase and feed the noble metal with oxygen when the O_2 partial pressure decreases [23,29–34].
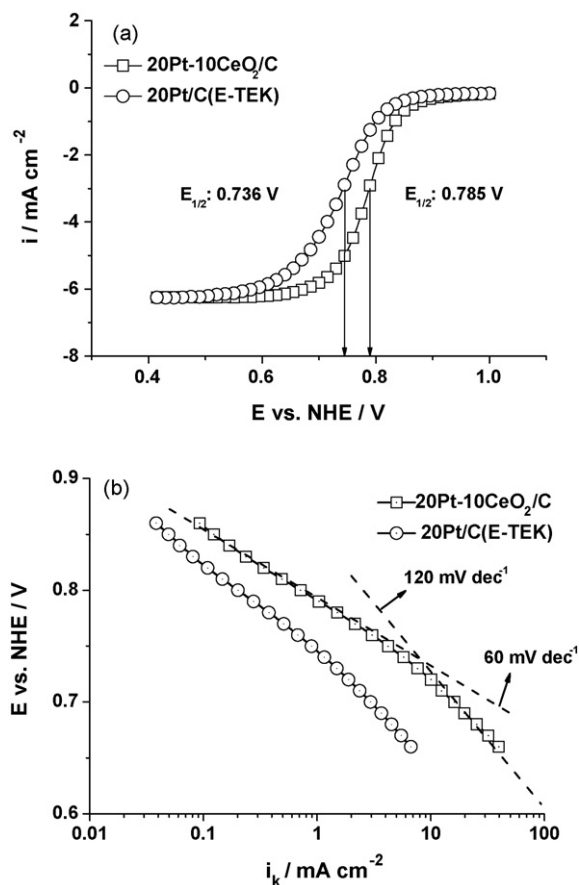
The Tafel plots obtained from the RDE voltammograms (Fig. 8b) are corrected for the effects of diffusion to give the kinetic currents in the mixed diffusion-kinetic current region, calculated from Eq. (1). Tafel plots generally show two different linear slopes with 60 mV dec^{-1} at high overpotentials (low current densities) and 120 mV dec^{-1} at low overpotentials (high current densities) in acid solution [46,47]. Two kinds of slope values are a consequence of the surface coverage by chemisorbed oxygenated species, which follow a Tempkin isotherm (high coverage) at low overpotentials and Langmuir isotherm (low coverage) at high overpotentials [46,47]. Fig. 8b shows the corresponding Tafel plots of the 20Pt–10CeO_2/C and commercial 20Pt/C catalysts. As expected, the kinetic of the electrochemical reaction for the 20Pt–10CeO_2/C catalyst is higher than that of the commercial 20Pt/C catalyst at all potentials. This indicates that the addition of CeO_2 into the Pt/C catalyst plays a synergistic role with Pt/C in the ORR.
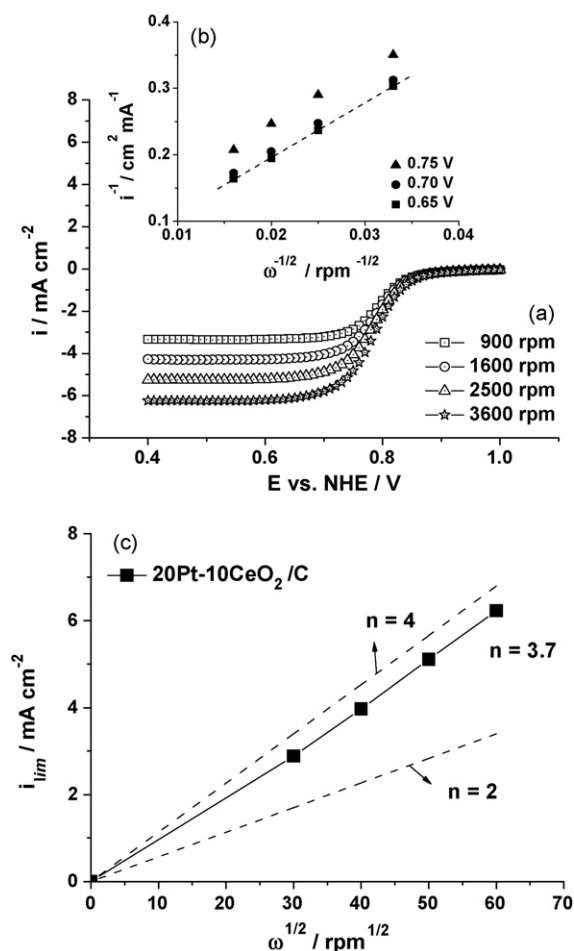
The ORR current density is corrected for diffusion limitation to obtain the kinetic current density using [13,21]:

$$I_{kim} = \frac{I_{lim} \cdot I_{ORR}}{I_{lim} - I_{ORR}}, \qquad (1)$$

where I_{kin} is the kinetic current density, I_{ORR} is the measured ORR current density, and I_{lim} is the limiting current density. Here, I_{lim} is the ORR current density at 0.4 V (vs. NHE).

Table 2 shows the kinetic current densities per milligram and EAS of Pt metal for the 20Pt–10CeO_2/C catalyst in comparison to the commercial 20Pt/C catalyst. The mass- and area-normalized kinetic current density at 0.75 V for the 20Pt–10CeO_2/C catalyst is about 4-folds that of the commercial 20Pt/C catalyst. Thus, the catalytic activity of 20Pt–10CeO_2/C catalyst for the ORR, based on the mass- and area-normalized kinetic current densities, is higher than that of the commercial 20Pt/C catalyst. This can be attributed to a synergistic effect between Pt and CeO_2, where CeO_2 acts as an oxygen storage component to increase the local oxygen concentration. CeO_2 is known to have the ability to act as an oxygen buffer, because it can release oxygen reversibly [22,23,29–34]. When CeO_2 nanoparticles are located in the vicinity of Pt nanoparticles, it is expected that CeO_2 will facilitate oxygen transfer to Pt nanoparticles, resulting in much better catalytic activity for the ORR. Consequently, the Pt nanoparticles in the vicinity may receive additional oxygen from the CeO_2 nanoparticles. Table 2 summarizes the electrokinetic parameters of the 20Pt–10CeO_2/C and commercial 20Pt/C catalysts.

RDE voltammograms are made to study the kinetics of the ORR for the 20Pt–10CeO_2/C catalyst. The I–V curves for the ORR are obtained at four rotation frequencies from 900 rpm to 3600 rpm at a scan rate of 50 mV s^{-1} (Fig. 9a). An increasing reduction current is observed when sweeping the potential to low values until reaching a limiting current. The oxygen reduction is fast enough that a flat limiting current at high overpotential is observed for the 20Pt–10CeO_2/C and commercial 20Pt/C catalysts. A flat limiting current can be explained, given the distribution of the active sites on the electrode surfaces. When the distribution of Pt nanoparticles is not good and the oxygen reaction is slower, the current plateau should be more inclined, as reported by Suarez-Alcantara et al. [48]. An increase in the rotation rate of the RDE resulted in an increase of the limiting current due to an increase in the availability of oxygen at the electrode surface. The currents of the ORR in the mixed kinetic-diffusion controlled region are analyzed in the form of Koutecky–Levich plots for different electrode rotation rates at 0.65 V, 0.70 V, and 0.75 V (Fig. 9b). In those plots, the inverse of the ORR current density (i^{-1}) is plotted versus the inverse of the square of the rotation velocity ($\omega^{-1/2}$). Linear lines can be fitted through the I–V curves of the ORR (Fig. 9b), which confirms that the ORR is proportional to the supply of oxygen from the electrolyte to the

Fig. 8. (a) ORR polarization curves and (b) Tafel plots obtained on the 20Pt–10CeO_2/C and commercial 20Pt/C(E-TEK) catalysts in 0.5 mol l^{-1} H_2SO_4 saturated with pure oxygen. Scan rate = 50 mV s^{-1} at 3600 rpm.

Fig. 9. (a) I–V curves for ORR on the 20Pt–10CeO$_2$/C catalyst obtained at four different rotation frequencies from 900 rpm to 3600 rpm at a scan rate of 50 mV s^{-1}, (b) Koutecky–Levich plots on the 20Pt–10CeO$_2$/C catalyst at different potentials and (c) Levich plot on the 20Pt–10CeO$_2$/C catalyst at limiting current for different rotation frequencies obtained from I–V curves in Fig. 9a.

surface of the RDE, as expected from the Levich model. This behavior indicates that the ORR is first order with respect to the concentration of reactant species. The currents of the ORR can be related to the kinetic current and the diffusion limited current using:

$$\frac{1}{i} = \frac{1}{i_k} + \frac{1}{i_d} = \frac{1}{i_k} + \frac{1}{B\omega^{1/2}}, \qquad (2)$$

where B is the Levich constant, ω is the electrode rotation rate, and i and i_k are the measured current and the kinetic current at a given electrode potential, respectively. i_d is the diffusion limited current density, ω is electrode rotation rate in unit of rpm.

B can be used to obtain the number of electrons involved in the ORR, using the Levich equation:

$$B = 0.62nFD_O^{2/3}\nu^{-1/6}C_O, \qquad (3)$$

where n is the number of electrons transferred per molecule of oxygen in the overall reaction, F is the Faraday constant, D_O is the diffusion coefficient of oxygen (1.9×10^{-5} cm^2 s^{-1}), and ν is the viscosity of the electrolyte (1.0×10^{-2} cm^2 s^{-1}). C_O is the bulk concentration of dissolved oxygen in diluted aqueous sulfuric acid (1.1×10^{-6} mol cm^{-3}). The Kotecky-Levich plots were used to determine B via the slope. According to the value reported by Ye and Crooks [49], the theoretical B calculated with the parameters described above by assuming $n = 4$ is 0.130 mA cm^{-2} rpm$^{-1/2}$. This

value can be compared to the measured value of B obtained from the slopes of the Koutecky–Levich plots in Fig. 9b. The value of B from the slopes of the plots in Fig. 9b is 0.124 ± 0.001 mA cm^{-2} rpm$^{-1/2}$, taking into account the fact that the current density is related to the geometric area of the electrode surface. Fig. 9c represents the plot of the limiting current (i_{lim}) as a function of the square root of the rotation velocity ($\omega^{1/2}$), the so-called Levich plot. The number of electrons calculated for the 20Pt–10CeO$_2$/C catalyst is ca. 3.7, which indicates a preferential four-electron transfer reaction. Since the values of the experimental and theoretical slopes are very similar, we suggest that the oxygen reduction in the sulfuric acid electrolyte solution proceeded via an overall four-electron transfer reaction, in which an oxygen molecule is reduced directly to water and peroxide formation is very small.

3.3. Single cell performances

In order to understand the enhanced performance of the Pt/C catalyst in the presence of CeO$_2$ as an oxygen storage component, single cell tests are carried out for the MEA made with the 20Pt–10CeO$_2$/C catalyst (0.3 mg cm^{-2}) as the cathode, and the commercial 20Pt/C catalyst (0.3 mg cm^{-2}) as the anode for H$_2$/O$_2$. For the sake of comparison, the I–V characteristic of the MEA made with the commercial 20Pt/C (0.3 mg cm^{-2}) as the anode and cathode are also prepared. From the I–V characteristics (Fig. 10), the open circuit voltages (OCV) of the single cells using the 20Pt–10CeO$_2$/C and commercial 20Pt/C catalysts are almost the same ($\sim$0.98 V). However, the 20Pt–10CeO$_2$/C catalyst shows a lower polarization loss than the commercial 20Pt/C catalyst. The peak power densities for the 20Pt–10CeO$_2$/C and commercial 20Pt/C catalysts are 0.58 W cm^{-2} and 0.49 W cm^{-2} at current densities of 1.01 A cm^{-2} 2 and 0.95 A cm^{-2}, respectively.

The Tafel slopes of the 20Pt–10CeO$_2$/C catalyst (65.5 mV dec^{-1}) are similar to that of the commercial 20Pt/C catalyst (69.6 mV dec^{-1}), which are close to the typical values (60 mV dec^{-1}) expected on a Pt electrode [50]. Due to the similarity of the Tafel slopes, this suggests that there is no change in the rate determining step for the ORR on the 20Pt–10CeO$_2$/C catalyst despite the differences in the electrocatalytic activities of 20Pt–10CeO$_2$/C and commercial 20Pt/C catalysts. Also, the current density at 900 mV for the 20Pt–10CeO$_2$/C catalyst is clearly higher when compared to the commercial 20Pt/C catalyst. As identified in the ORR, the 20Pt–10CeO$_2$/C catalyst has better performance and a higher power density than the commercial 20Pt/C catalyst in the I–V characteristics. This is due to the oxygen storage capacity of CeO$_2$ and its ability to exchange oxygen rapidly with oxygen in the buffer. This implies that the difference is attributed to the addition
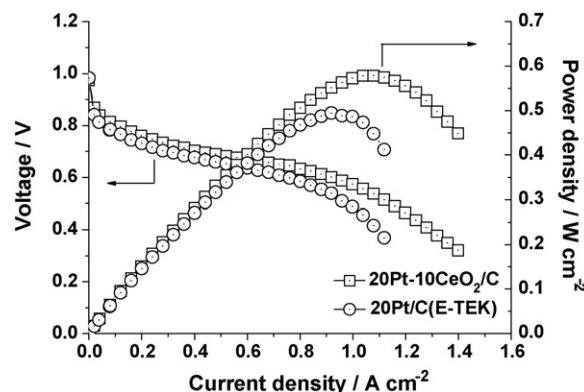
Fig. 10. Cell voltage and power density as a function of current density for the single cell with a commercial 20Pt/C(E-TEK) catalyst (anode) and 20Pt–10CeO$_2$/C catalyst (cathode) operating with humidified H$_2$/O$_2$ gases at 80 °C and 1 atm. The catalyst loading of anode and cathode was both 0.3 mg cm^{-2}.

Table 3
Kinetic parameters for the ORR on the 20Pt–10CeO$_2$/C and commercial 20Pt/C catalysts from the single cell at 80 °C and 1 atm.

Sample	$i_{900\,mV}$ (mA cm^{-2})	$i_{900\,mV}$ (mA mg^{-1}Pt)	Kinetic parameter	
			E_0 (mV)	b (mV dec^{-1})
20Pt/C(E-TEK)	11.7	534.2	983	69.6
20Pt–10CeO$_2$/C	14.0	663.0	974	65.5

of CeO$_2$ into the Pt/C catalyst, which plays a synergistic role with Pt/C in the ORR. Table 3 summarizes the kinetic parameters for the ORR on the 20Pt–10CeO$_2$/C and commercial 20Pt/C catalysts from the single cell performance.

A reasonable mechanism for improving cell performance is through the addition of CeO$_2$ into the Pt/C catalyst as a cathode. As shown in Fig. 11, we propose a reasonable mechanism for

providing additional oxygen from CeO$_2$ nanoparticles to the Pt active sites at the cathode. First of all, in order to propose a hypothesis regarding synergistic effect, Pt and CeO$_2$ particles must be well-dispersed and as small as possible in order to have a large contact area between the particles. CeO$_2$ particles also need to be in contact with Pt active sites in order to successfully supply additional oxygen. Thus, an effective ORR would occur at the interfaces of Pt and CeO$_2$ nanoparticles, where additional oxygen could be provided, leading to enhanced fuel cell performance. According to its redox properties, CeO$_2$ nanoparticles can store oxygen during an oxygen-rich phase and feed the Pt catalyst with oxygen when the oxygen partial pressure decreases [22,23,29–34]. We propose the following explanation relating to the redox property of CeO$_2$ under the fuel cell condition. Oxygen on the surface of the CeO$_2$ is released to the closed Pt active sites when CeO$_2$ changes to Ce$_2$O$_3$, which increases the local oxygen
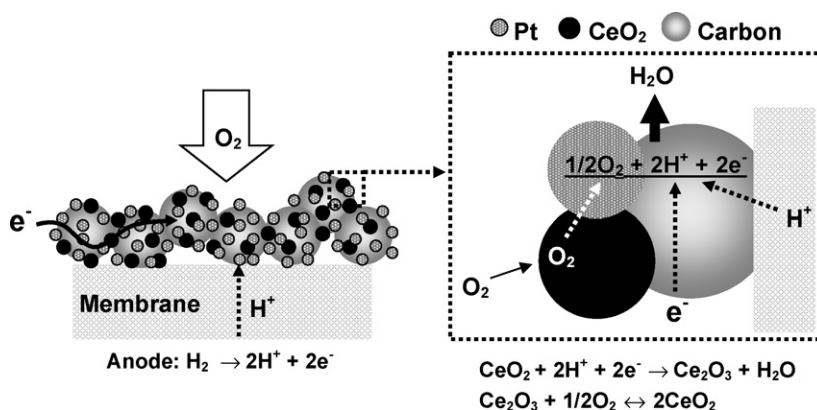

Fig. 11. A reasonable mechanism of CeO$_2$ addition into the Pt/C catalyst for improving ORR.
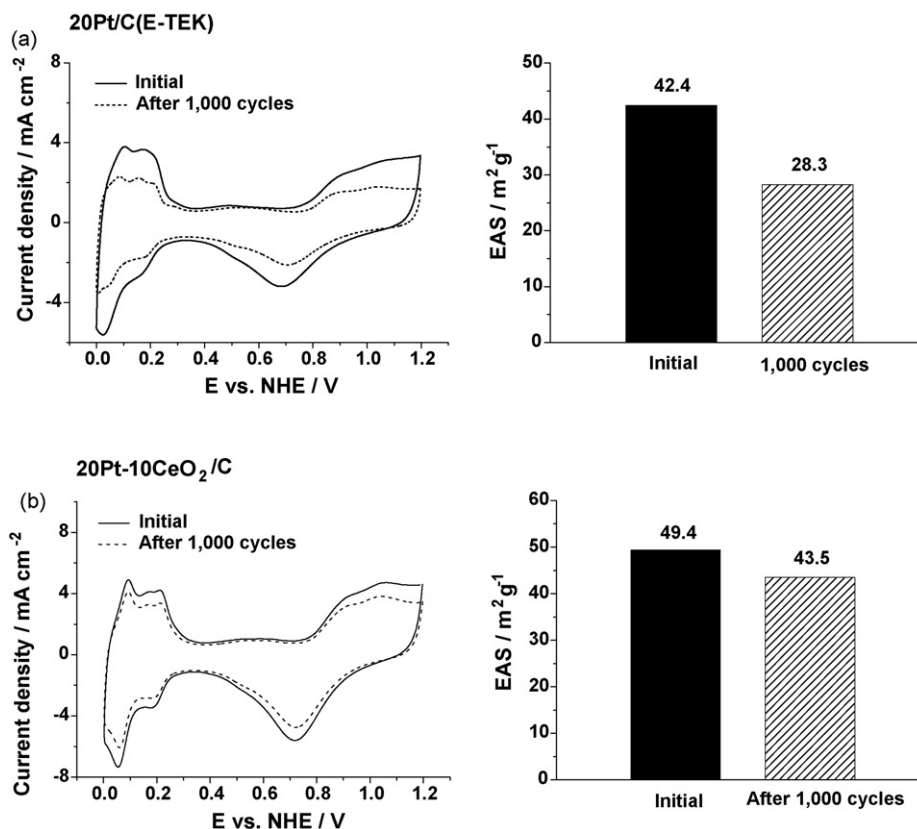

Fig. 12. Cyclic voltammograms of H$_2$ adsorption/desorption on the (a) commercial 20Pt/C(E-TEK) and (b) 20Pt–10CeO$_2$/C catalysts before and after 1000 potential cycles in 0.5 mol l^{-1} H$_2$SO$_4$ solution at room temperature with a scan rate of 50 mV s^{-1}.

concentration. Subsequently, Ce_2O_3 quickly changes to CeO_2 in the cathode atmosphere. The key role of CeO_2 in this catalyst system is the ability of cerium ion to switch between the Ce^{4+} and Ce^{3+} as follows [51]:

$$CeO_2 \Leftrightarrow CeO_{2-x} + \frac{x}{2}O_2 \quad (0 \leq x \leq 0.5). \tag{4}$$
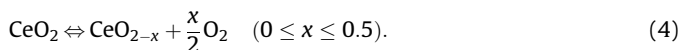
Lee et al. [23] reported that the oxygen ions adsorbed on Ce^{3+} sites with oxygen vacancies would be transferred to the Pt active sites, while the oxidation state of Ce is reversibly changed from Ce^{4+} to Ce^{3+}. Also, Xu et al. [34] insisted that the change in the redox states between Ce_2O_3 and CeO_2 is responsible for the oxygen storage. Since CeO_2 has the ability to store oxygen, it may provide some additional oxygen to Pt, especially when oxygen concentration is low in the high current density region [34]. In fact, CeO_2 has been used as an electrolyte in high temperature fuel cell such as solid oxide fuel cell due to high oxygen transfer ability, originated from its oxygen defects [52]. Although the oxygen storage rate of CeO_2 is a little slow at temperature below 100 °C, CeO_2 can transfer additional oxygen to adjacent Pt catalyst in the cell operating condition (∼80 °C). Therefore, the oxygen supply rate to the Pt catalyst is one of the major factors that could affect the ORR kinetics in the cathode. Fast supply of oxygen to the Pt catalyst could reduce the high overpotential at the cathode, leading to an enhanced cell performance. Especially, as CeO_2 added into the Pt/C catalyst provides additional oxygen to the Pt active sites at lower cell voltages (e.g. higher current density), it could be effectively reduced the mass transfer polarization. However, we do not know how much additional oxygen can be stored and how fast the oxygen will be released to supply the closed Pt catalyst. Further work is underway to address this important aspect.

3.4. Accelerated durability tests

Accelerated durability tests (ADTs) of the 20Pt–10CeO_2/C and commercial 20Pt/C catalysts are carried out by continuously applying potentials between 0 V and 1.2 V at 50 mV s^{-1} in 0.5 mol l^{-1} H_2SO_4 solution. In general, the durability of Pt-based electrocatalyst is tested by performing the potential cycling as accelerated durability test in diluted acidic solution. The voltammograms of H_2 adsorption/desorption is used to determine the change of the Pt active surface area for the 20Pt–10CeO_2/C and commercial 20Pt/C catalysts by measuring H_2 desorption regions before and after 1000 potential cycles (Fig. 12). It can be seen from Fig. 12a that the EAS value for the commercial 20Pt/C catalyst decreases rapidly from 42.4 m^2 g^{-1} to 28.3 m^2 g^{-1} after the ADT (about 33.3%), indicating a notable decrease of the Pt active surface area due to Pt sintering, the oxidation of the carbon support, and the dissolution of Pt metal [7,21]. While the EAS value for the 20Pt–10CeO_2/C catalyst after the ADT decreases from 49.4 m^2 g^{-1} to 43.5 m^2 g^{-1} with no significant variation (about 11.9%), indicating no considerable decrease of the Pt active surface area (Fig. 12b). Thus, the degradation rate of the 20Pt–10CeO_2/C catalyst is smaller than that of the commercial 20Pt/C catalyst. This clearly indicates that the 20Pt–10CeO_2/C catalyst is significantly more durable in the acidic solution compared to the commercial 20Pt/C catalyst.

The durability of the catalytic activity was also tested by measuring the $E_{1/2}$ for ORR before and after ADTs performed at 25 °C in a 0.5 mol l^{-1} H_2SO_4 electrolyte solution saturated with oxygen using RDE at a rotation rate of 3600 rpm, as shown in Fig. 13. It can be seen from Fig. 13a that the $E_{1/2}$ for the commercial 20Pt/C catalyst after the ADT shows a significant anodic shift of 72 mV in the mixed kinetic-diffusion controlled region. This is due to the remarkable decrease of the Pt active sites. On the other hand,
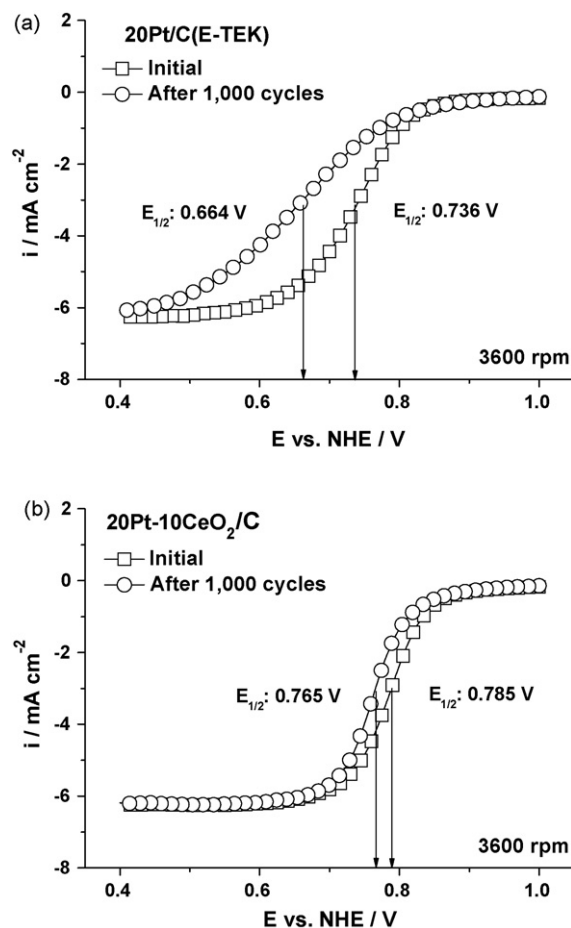
Fig. 13. ORR polarization curves obtained on the (a) commercial 20Pt/C(E-TEK) and (b) 20Pt–10CeO_2/C catalysts before and after 1000 potential cycles in 0.5 mol l^{-1} H_2SO_4 saturated with pure oxygen. Scan rate = 50 mV s^{-1} at 3600 rpm.

the $E_{1/2}$ for the 20Pt–10CeO_2/C catalyst shows a small degradation of 20 mV over 1000 potential cycles because the EAS value does not decrease significantly during potential cycling (Fig. 13b). As expected, the trend of ORR activities is remarkably similar to that of the EAS loss seen after potential cycling experiment.

As described above, we observed that the 20Pt–10CeO_2/C catalyst had high durability in acidic solution by the potential cycling experiment, while the commercial 20Pt/C catalyst was seriously deactivated in the same condition. This result was confirmed by observing the changes of the Pt particle sizes in both catalysts before and after ADTs with the TEM images. Fig. 14 depicts the TEM images of the 20Pt–10CeO_2/C and commercial 20Pt/C catalysts before and after ADTs. As shown in Fig. 14a and b, the particle size of the commercial 20Pt/C catalyst was increased from 2.6 nm to 5.7 nm after the ADT. Thus, the main reason for the decrease in the Pt active surface area is confirmed to be the sintering of the Pt particles as evident from the TEM images. Zaragoza-Martin et al. [53] reported that the decrease of the Pt surface area is due to the aggregation of Pt particles, which can be produced by the applied potential and the oxidation of the carbon support. On the other hand, the TEM image of the 20Pt–10CeO_2/C catalyst depicts a slight increase of particle size from 3.2 nm to 4.4 nm after the ADT (Fig. 14c and d). The increase of the particle size in the 20Pt–10CeO_2/C catalyst is very small compared to that of the commercial 20Pt/C catalyst. We can conclude that the existence of CeO_2 in the Pt/C catalyst is likely prevents the agglomeration and dissolution of Pt particles on the carbon support, and thus has more stability in acidic solution, e.g. more catalytic durability, in the fuel cell operating condition.
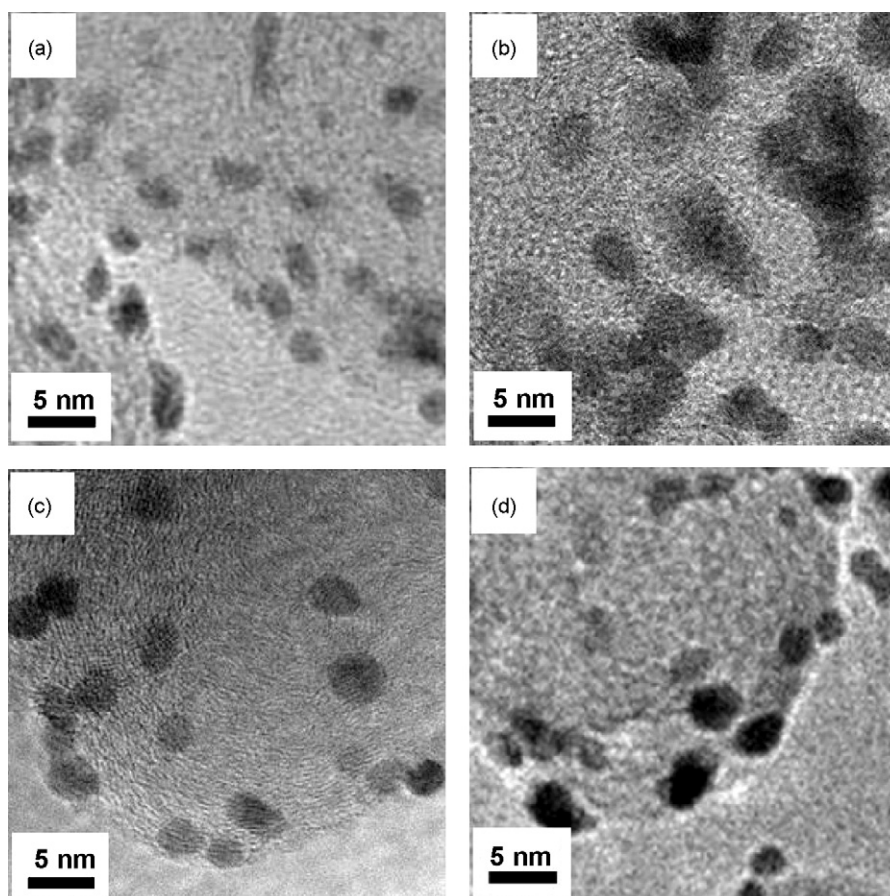
Fig. 14. TEM images of the (a and b) commercial Pt/C(E-TEK) and (c and d) 20Pt–10CeO$_2$/C catalysts (a and c) before and (b and d) after 1000 potential cycles.

The new synthesis used in this study provides an easy and reproducible procedure for subsequent preparation of Pt and CeO$_2$ nanoparticles, supported on carbon. As suggested by our previous results, it is reasonable to expect that, in a low-temperature fuel cell, the addition of CeO$_2$ into a Pt/C catalyst should boost ORR activity and interrupt the agglomeration of Pt nanoparticles, and hence increase the cell performance and durability.

4. Conclusions

Highly dispersed Pt–CeO$_2$/C catalyst, with particle size ranging from 3 nm to 5 nm, were successfully synthesized by a continuous two-step process. Both XRD and TEM results, the diffraction pattern of the 20Pt–10CeO$_2$/C catalyst revealed that both crystalline Pt and CeO$_2$ phases coexisted. It was found that the Pt and CeO$_2$ nanoparticles were uniformly dispersed on the edge of their carbon support and CeO$_2$ nanoparticles can be found near Pt nanoparticles. When CeO$_2$ nanoparticles are located in the vicinity of Pt nanoparticles, CeO$_2$ nanoparticles might facilitate oxygen transfer to Pt nanoparticles, resulting in much better the ORR activity (synergistic effect). Based on the polarization curves for the ORR, the optimum proportion of CeO$_2$ into the 20Pt/C catalyst was 10 wt%. In the ORR and single cell tests, the 20Pt–10CeO$_2$/C catalyst showed higher performance than the commercial 20Pt/C catalyst, due to the oxygen storage capacity of CeO$_2$ and its ability to exchange oxygen rapidly with oxygen in the buffer. The ADT result for 20Pt–10CeO$_2$/C catalyst showed no significant variation (about 11.9%) in sulfuric acid, indicating no considerable decrease of the Pt active surface area. This was due to the existence of CeO$_2$, which prevented the agglomeration and dissolution of Pt particles on the carbon support. A continuous two-step process used in this study

provided an easy and reproducible procedure for the preparation of Pt and CeO$_2$ nanoparticles supported on carbon. Thus, we can conclude that the 20Pt–10CeO$_2$/C catalyst, which had the predominant activity and durability, may be a good alternative as a cathode for low-temperature fuel cell.

References

[1] J. Larminei, A. Dicks, Fuel Cell Systems Explained, 2nd ed., John Wiley & Sons, Chichester, 2003 .
[2] J. Wheldon, W.-J. Lee, D.-H. Lim, A.B. Broste, M. Bollinger, W.H. Smyrl, Electrochem. Solid-State Lett. 12 (2009) B86.
[3] D.-H. Lim, D.-H. Choi, W.-D. Lee, H.-I. Lee, Appl. Catal. B: Environ. 89 (2009) 484.
[4] D.-H. Lim, W.-D. Lee, H.-I. Lee, Catal. Surv. Asia 12 (2008) 310.
[5] Y. Shao, J. Sui, G. Yin, Y. Gao, Appl. Catal. B: Environ. 79 (2008) 89.
[6] H. Liu, W. Li, A. Manthiram, Appl. Catal. B: Environ. 90 (2009) 184.
[7] J. Wang, G. Yin, Y. Shao, S. Zhang, Z. Wang, Y. Gao, J. Power Sources 171 (2007) 331.
[8] S. Takenaka, H. Matsumori, H. Matsune, E. Tanabe, M. Kishida, J. Electrochem. Soc. 155 (2008) B929.
[9] D.-H. Lim, L. Lu, D.-B. Kim, D.-H. Choi, D.-R. Park, H.-I. Lee, J. Nanopart. Res. 10 (2008) 1215.
[10] D.-H. Lim, W.-D. Lee, D.-H. Choi, D.-R. Park, H.-I. Lee, J. Power Sources 185 (2008) 159.
[11] C. Wang, M. Waje, X. Wang, J.M. Tang, R.C. Haddon, Y. Yan, Nano Lett. 4 (2004) 345.
[12] H.A. Gasteiger, S.S. Kocha, B. Sompalli, F.T. Wangner, Appl. Catal. B: Environ. 56 (2005) 9.
[13] K.-W. Park, Y.-E. Sung, J. Ind. Eng. Chem. 12 (2006) 165.
[14] J.-S. Choi, W.-S. Chung, H.-Y. Ha, T.-H. Lim, I.-H. Oh, S.-A. Hong, H.-I. Lee, J. Power Sources 156 (2006) 466.

[15] D.-H. Lim, D.-H. Choi, D.-W. Lee, D.-R. Park, H.-I. Lee, Electrochem. Solid-State Lett. 10 (2007) B87.
[16] C. Kim, H.-H. Kwon, I.-K. Song, Y.-E. Sung, W.-S. Chung, H.-I. Lee, J. Power Sources 171 (2007) 404.
[17] F. Wen, U. Simon, Chem. Mater. 19 (2007) 3370.
[18] R. Bashyam, P. Zelenay, Nature 443 (2006) 63.
[19] M.H. Shao, K. Sasaki, R.R. Adzic, J. Am. Chem. Soc. 128 (2006) 3526.
[20] J. Zhang, K. Sasaki, E. Sutter, R.R. Adzic, Science 315 (2007) 220.
[21] V.R. Stamenkovic, B. Fowler, B.S. Mun, G. Wang, P.N. Ross, C.A. Lucas, N.M. Markovic, Science 315 (2007) 493.
[22] D.-H. Lim, W.-D. Lee, D.-H. Choi, H.-H. Kwon, H.-I. Lee, Electrochem. Commun. 10 (2008) 592.
[23] K.H. Lee, K. Kwon, V. Roev, D.Y. Yoo, H. Chang, D. Seung, J. Power Sources 185 (2008) 871.
[24] L. Xiong, A. Manthiram, Electrochim. Acta 50 (2005) 2323.
[25] J.R.C. Salgado, E. Antolini, E.R. Gonzalez, Appl. Catal. B: Environ. 57 (2005) 283.
[26] F.H.B. Lima, J.R.C. Salgado, E.R. Gonzalez, E.A. Ticianelli, J. Electrochem. Soc. 154 (2007) A369.
[27] S. Mukerjee, S. Srinivasan, M.P. Soriaga, J. Phys. Chem. 99 (1995) 4577.
[28] V.R. Stamenkovic, T.J. Schmidt, P.N. Ross, N.M. Markovic, J. Phys. Chem. B 106 (2002) 11970.
[29] Y. Liu, A. Ishihara, S. Mitsushima, N. Kamiya, K.I. Ota, Electrochem. Solid-State Lett. 8 (2005) A400.
[30] D.-H. Lim, W.-J. Lee, N.L. Macy, W.H. Smyrl, Electrochem. Solid-State Lett. 12 (2009) B123.
[31] H.-B. Yu, J.-H. Kim, H.-I. Lee, M.A. Schibioh, J.-Y. Lee, J.-H. Han, S.-P. Yoon, H.-Y. Ha, J. Power Sources 140 (2005) 59.
[32] E. Antolini, E.R. Gonzalez, Solid State Ionics 180 (2009) 746.
[33] K. Kuwaha, A. Matsuoka, Japan Patent 10-55807 (1998).

[34] Z. Xu, Z. Qi, A. Kaufman, J. Power Sources 115 (2003) 40.
[35] J. Shim, C.-R. Lee, H.-K. Lee, J.-S. Lee, E.J. Cairns, J. Power Sources 102 (2001) 172.
[36] L. Xiong, A. Manthiram, Electrochim. Acta 49 (2004) 4163.
[37] W.-S. Shin, C.-R. Jung, J.-H. Han, S.-W. Nam, T.-H. Lim, S.-A. Hong, H.-I. Lee, J. Ind. Eng. Chem. 10 (2004) 302.
[38] Q. Fu, H. Saltsburg, M. Flytzani-Stephanopoulos, Science 301 (2005) 935.
[39] B.I. Anatoly, J.G. Nunan, US Patent 6,387,338 (2002).
[40] M.A. Scibioh, S.-K. Kim, E.A. Cho, T.-H. Lim, S.-A. Hong, H.Y. Ha, Appl. Catal. B: Environ. 84 (2008) 773.
[41] C. Laberty-Robert, J.W. Long, E.M. Lucas, K.A. Pettigrew, R.M. Stroud, M.S. Doescher, D.R. Rolison, Chem. Mater. 18 (2006) 50.
[42] J.C. Serrano-Ruiz, A. Sepúlveda-Escribano, F. Rodríguez-Reinoso, D. Duprez, J. Mol. Catal. A: Chem. 268 (2007) 227.
[43] S. Letichevsky, C.A. Tellez, R.R. de Avillez, M.I.P. da Silva, M.A. Fraga, L.G. Appel, Appl. Catal. B: Environ. 58 (2005) 203.
[44] H.C. Yao, Y.F.Y. Yao, J. Catal. 86 (1984) 254.
[45] Y.-G. Yoon, T.-H. Yang, G.-G. Park, W.-Y. Lee, C.-S. Kim, J. Power Sources 118 (2003) 189.
[46] N.M. Markovic, T.J. Schmidt, V. Stamenkovic, P.N. Ross, Fuel Cells 1 (2001) 105.
[47] V.S. Murthi, R.C. Urian, S. Mukerjee, J. Phys. Chem. B 108 (2004) 11011.
[48] K. Suarez-Alcantara, A. Rodriguez-Castellanos, R. Dante, O. Soloraza-Feria, J. Power Sources 157 (2006) 114.
[49] H. Ye, R.M. Crooks, J. Am. Chem. Soc. 129 (2007) 3627.
[50] J. Perez, E.R. Gonzalez, E.A. Ticianelli, Electrochim. Acta 44 (1998) 1329.
[51] J. Zhao, W. Chen, Y. Zheng, Mater. Chem. Phys. 113 (2009) 591.
[52] A.D. Mayemic, M.J. Janik, J. Phys. Chem. C 112 (2008) 14955.
[53] F. Zaragoza-Martin, D. Sopena-Escario, E. Morallon, C. Salinas-Martinez de Lecea, J. Power Sources 171 (2007) 302.